ARTICLES
PUBLISHED ONLINE: 21 JUNE 2009 | DOI: 10.1038/NNANO.2009.143
nature nanotechnology

Phase-locking of magnetic vortices mediated by antivortices

A. Ruotolo*, V. Cros, B. Georges, A. Dussaux, J. Grollier, C. Deranlot, R. Guillemet, K. Bouzehouane, S. Fusil and A. Fert

Synchronized spin-valve oscillators may lead to nanosized microwave generators that do not require discrete elements such as capacitors or inductors. Uniformly magnetized oscillators have been synchronized, but offer low power. Gyrating magnetic vortices offer greater power, but vortex synchronization has yet to be demonstrated. Here we find that vortices can interact with each other through the mediation of antivortices, leading to synchronization when they are closely spaced. The synchronization does not require a magnetic field, making the system attractive for electronic device integration. Also, because each vortex is a topological soliton, this work presents a model experimental system for the study of interacting solitons.

A magnetic vortex is a flux-closure magnetic state that consists of a curling in-plane magnetization and an out-of-plane vortex core[1,2]. It can represent the lowest-energy configuration of a single-domain magnet or be nucleated by a circular magnetic field. This magnetic configuration shows a very rich dynamic behaviour. Among the accessible modes that may be excited, the circular motion of the core around its equilibrium position, called gyrotropic precession, has attracted a large amount of interest[3]. This mode can be excited by a spin-polarized current through the transfer of spin-angular momentum to the local magnetic moment, a phenomenon called spin transfer torque[4,5].

Spin transfer torque has been routinely used to control the orientation of magnetic nanostructures[6,7]. It can also drive the magnetic orientation of a layer into an oscillation, creating a spin transfer nano-oscillator (STNO)[8,9]. Its use in exciting a magnetic vortex in spin-valve nanocontacts[10,11] has attracted interest because in this vortex-based STNO, a large part of the magnetoresistance is transformed into power. As a consequence, the power is much larger than that generated by uniform-mode STNOs, although the maximum frequency is lower (<2 GHz). The synchronization of two closely spaced STNOs with uniform excitation modes has been demonstrated through spin–wave coupling, leading to significant improvements in their output features[12,13].

Here we demonstrate that local synchronization is possible between vortex-based STNOs. We show that vortices orbiting beneath closely spaced nanocontacts can synchronize through the mediation of antivortices. As in the case of phase-locking between uniform modes, the phase-locked state is characterized by decreased linewidth and increased power. Remarkably, the best condition for phase-locking in the system presented here is the absence of externally applied magnetic field. The mechanism of phase coupling is interpreted by using a simple analytical model and on the basis of the results of micromagnetic simulations for the dynamics of interacting vortices and antivortices.

An integrated array of nano-oscillators

In our study we nucleated magnetic vortices under a 2 × 2 array of nanocontacts with centre-to-centre spacing d, as shown in Fig. 1. We prepared devices with $d = 10$ μm, 2 μm and 500 nm. The magnetic structure was a sputtered deposited multilayer consisting of a

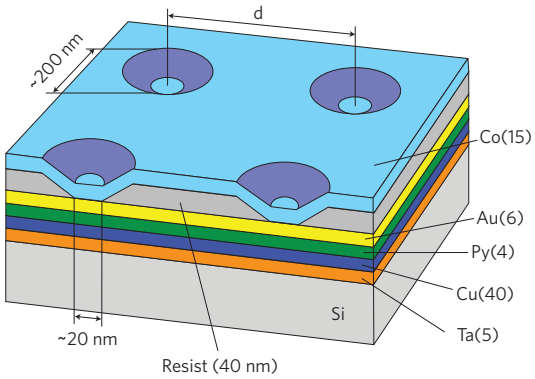

Figure 1 | The studied system. Schematic (not to scale) of the integrated array of 2 × 2 nanocontacts with intercontact distances d. The Py (4 nm) polarizer is deposited on a Ta(5 nm)/Cu(40 nm) seed bilayer. The Co (15 nm) active layer is deposited after opening the holes into the resist (40 nm) previously spun on the Au (6 nm) spacer. The holes, opened by a conductive-tip AFM, have a bottom diameter of ~20 nm and a top diameter of ~200 nm. As is clear from the cross-section of the two front contacts, the device area is only determined by the bottom diameter.

5-nm tantalum/40-nm copper/4-nm permalloy (Py) bottom electrode, a 6-nm gold spacer and a 15-nm cobalt/100-nm gold top electrode. The thickness of the ferromagnetic layers were chosen in such a way as to favour nucleation of vortices in the cobalt layer. The nanoholes were opened by conductive tip atomic force microscope (AFM) nano-indentation and plasma etching[14] into a 40-nm resist spun on the spacer layer before depositing the top electrode. A diameter of ~20 nm could be estimated for the contacts by AFM scan. The lithographically defined top electrode connected the four contacts in parallel. The dynamics of this system could be probed by measuring the induced radio-frequency signal produced at the electrodes because of the giant magnetoresistance effect.

In Fig. 2a, we display the power spectral density (PSD) for the device with intercontact distance $d = 2$ μm in an $H_\perp = +50$ mT perpendicular applied field. The field sign is defined according to the polarity of a previously applied large reset field (see Methods). To stabilize the initial magnetic configuration with a vortex at

Unité Mixte de Physique CNRS/Thales and Université Paris Sud 11, Route départementale 128, 91767 Palaiseau, France. *e-mail: antonio.ruotolo@mac.com

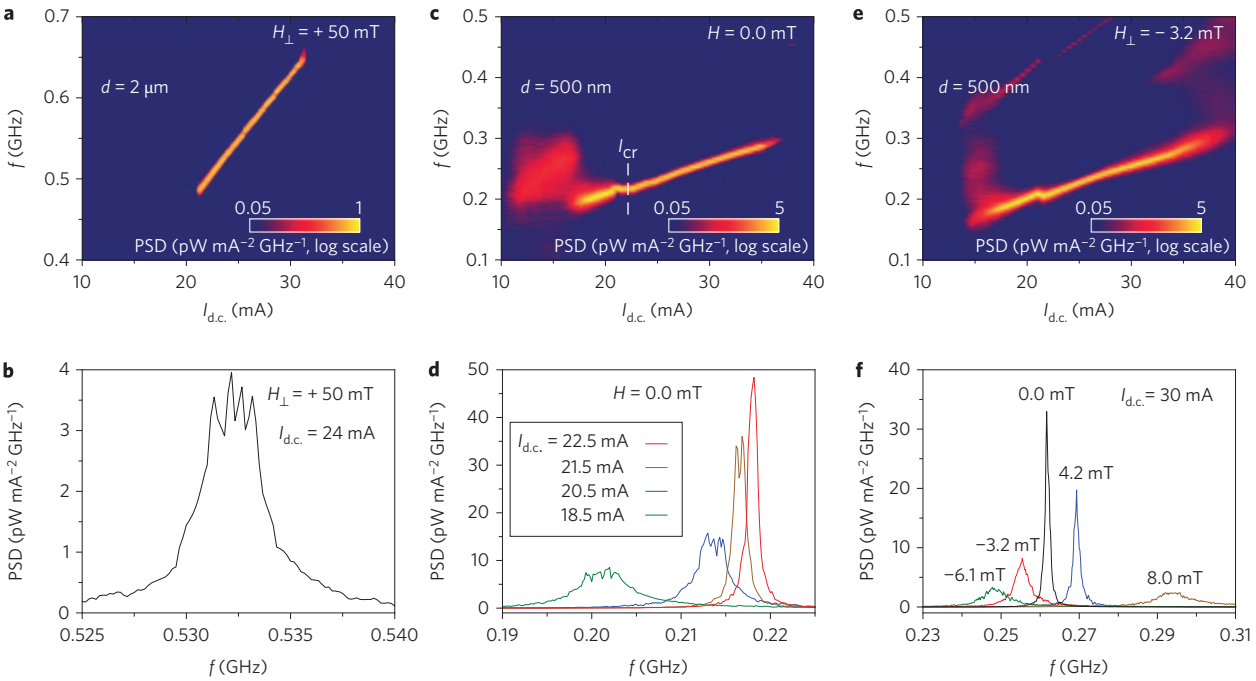

Figure 2 | Power outputs of arrays of 2 × 2 nanocontacts with different intercontact distances. a, Map of power spectrum amplitude versus frequency and applied current bias $I_{d.c.}$ of a matrix of 2 × 2, 2 μm-spaced nanocontacts. A field of 50 mT was applied perpendicular to the sample plane. **b**, Magnification of the power spectrum at a fixed $I_{d.c.}$ reveals that the spectrum is in fact the superposition of four independent spin transfer peaks whose relative frequency positions are constant with $I_{d.c.}$. **c**, When the intercontact distance is reduced to $d = 500$ nm, a knee can be observed in the map, below which the spectrum appears broader. **d**, The plots at fixed values of $I_{d.c.}$ reveal that, below the knee, the spectrum is still the superposition of four peaks. At the knee, the four peaks merge into two peaks and, above the knee, one single peak is observed. The critical current, defined as the current above which one single peak can be observed, is $I_{cr} = 22.0 \pm 0.5$ mA in zero field and changes with an external applied field. **e**, In the device with $d = 500$ nm, a similar behaviour is observed in the range $|H_\perp| < 10$ mT. **f**, The applied field reduces the peak amplitude and increases the linewidth.

each contact location, the maximum d.c. current $I_{d.c.} = 40$ mA was applied. The spectra were then recorded at decreasing d.c. current values. The plots at fixed $I_{d.c}$ (see Fig. 2b for $I_{d.c.} = 24$ mA) allow interpretation of the device output as the superposition of four signals generated by four independent (or weakly interacting) vortices orbiting around the contacts. Four peaks are seen to maintain their relative frequency positions through the whole current range. The small peak frequency differences are due to the unavoidable and uncorrelated differences in the nanocontacts size, which lead to slightly different currents flowing through the four contacts connected in parallel. Similar results have been obtained (not shown) for the 10-μm-spaced contacts.

The frequency increases with d.c. current (blueshift) with a tunability of $df/dI_{d.c.} = +15.7$ MHz mA^{-1} and $df/dI_{d.c.} = +19.6$ MHz mA^{-1} for the devices with $d = 2$ μm and $d = 10$ μm, respectively. At a fixed d.c. current, we observed an increase of the frequency with perpendicular applied field at a rate of $df/d\mu_0 H_\perp = +2.5$ MHz mT^{-1} and $df/d\mu_0 H_\perp = +2.3$ MHz mT^{-1} for the samples with $d = 2$ μm and $d = 10$ μm, respectively. Note that, for both the devices with $d = 2$ μm and 10 μm, no signal was detected at $H_\perp = 0$ mT, but we had to apply a few tens of mT with the same polarity as the reset field to sustain radio-frequency output. The total integrated power, numerically estimated as the area under the acquired spectrum, is 22 ± 2 nW A^{-2} in the case of intercontact spacing $d = 2$ μm and 23 ± 2 nW A^{-2} for $d = 10$ μm. The power is independent of $I_{d.c.}$ and $H_\perp$ in the studied range and not significantly dependent on d.

Phase-locking of closely spaced nano-oscillators

The spectrum map of the device with $d = 500$ nm (Fig. 2c) is much richer. It shows a knee below which four peaks can again be resolved. At larger bias currents, the four peaks merge into two peaks, over a small range of currents, and then into a single peak (Fig. 2d). The merging is accompanied by a sudden increase of the power amplitude and a significant narrowing of the linewidth (narrowest measured linewidth $\Delta f = 0.9$ MHz). Let us emphasize that the spectrum map shown in Fig. 2c was recorded in zero applied field. We define the critical current I_{cr} as the smallest current at which a single peak can be resolved in the spectrum. In zero field, $I_{cr} = 22.0 \pm 0.5$ mA and it changes with the applied field at a rate $dI_{cr}/d\mu_0 H_\perp = +0.1$ mA mT^{-1}.

The output was sustained in a field range around zero, typically for $|H_\perp|$ smaller than 10 mT (Fig. 2e and f), that is, in a range where gyrotropic precession was not observed in widely spaced ($d = 2$ and 10 μm) nanocontacts. The largest peak amplitude was recorded at $H = 0.0$ mT. An applied field always leads to a reduction of the peak amplitude and an increase of the linewidth, with the area underneath remaining constant, regardless of the sign of the field. The range of oscillating frequency is significantly lower than the one found for the widely spaced nanocontacts (see the range of oscillation frequencies in Fig. 2a and c). In fact, a frequency (in the centre of the four peaks) $f = 581.5$ MHz at $I_{d.c.} = 25$ mA and $H_\perp = 50$ mT for the case $d = 2$ μm should correspond, according to the measured tunability in field, to a frequency $f = 456.5$ MHz at $H_\perp = 0$ mT and at the same $I_{d.c.}$. This value is about twice the oscillating frequency in the closely spaced ($d = 500$ nm) nanocontacts at the same I_{dc}. Following this frequency behaviour, we also find that the tunability in current is reduced in the closely spaced device compared to the others to $df/dI_{d.c.} = +5.6$ MHz mA^{-1}.

From the spectra in Fig. 2d, we estimated an integrated power $P = 88 \pm 2$ nW A^{-2} for $I_{d.c.} > I_{cr}$. Just below I_{cr}, the total integrated power decreases suddenly to reach half the power at $I_{d.c.} = 18.5$ mA and keeps decreasing. This behaviour is similar to that observed for the unlocking of uniform modes in arrays of nanocontacts coupled through spin waves[12,13]. At much lower $I_{d.c.}$, where the remaining

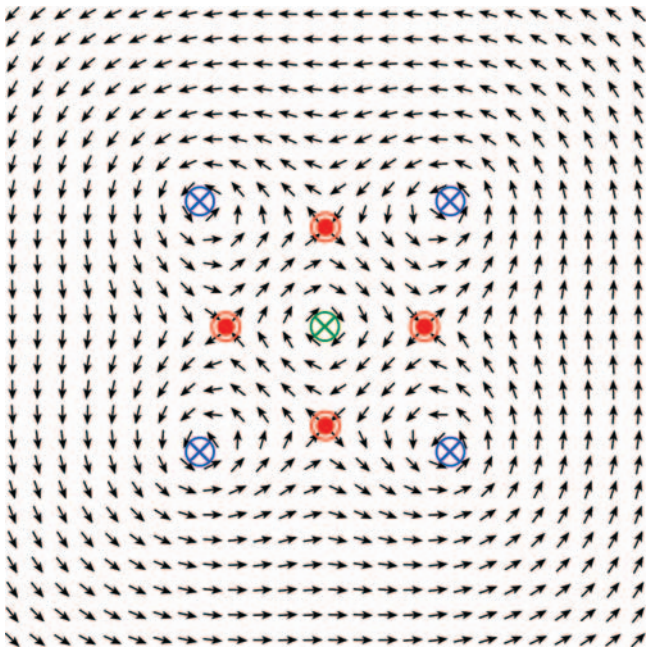

Figure 3 | Vortex–antivortex lattice ground state in zero field. The Oersted field generated by the current flowing through a matrix of 2×2 nanocontacts nucleates a vortex under each of them. Because all four vortices (blue) have the same chirality, energy minimization implies nucleation of antivortices (red) on the matrix sides and of a vortex with opposite chirality (green) in the matrix centre. Furthermore, minimization of magnetostatic energy implies magnetic flux closure through nearest-neighbour vortex–antivortex cores. Each vortex (antivortex) is surrounded by antivortices (vortices) with opposite core polarity. In the simulation the intercontact distance was $d = 500$ nm. The map shown is a detail of a simulation performed on a larger sample area ($2.5 \times 2.5\ \mu m^2$).

coupling should have vanished (below 16 mA in Fig. 2d), we clearly observe a significant reduction of the integrated power, most probably due to the fact that the single vortex oscillating modes are fading out and become unstable. This hinders us from making a quantitative comparison of the total integrated power between far below and above I_{cr}. A more accurate comparison is that made between the total integrated power at a given $I_{d.c.}$ in the three devices with different d. For $I_{d.c.} > I_{cr}$, the integrated power in the 500-nm-spaced nanocontacts is four times larger than that measured in both the widely spaced contacts. Our devices can be described as four resistances in parallel, connected in series with an external current source[12,15]. In this case, the behaviour we observe with respect to the integrated power in the $d = 500$ nm device can be associated with four phase-locked vortices orbiting around their nanocontacts with zero phase difference.

A vortex–antivortex lattice ground state

The starting point of our analysis is the determination of the ground state of the system in zero applied field, with the help of a micromagnetic simulation (Fig. 3). The application of an experimental maximum total current $I_{d.c.} = 40$ mA leads to the nucleation of four vortices under the contacts (one vortex for each contact). The vortices are nucleated in the potential wells of the Oersted field generated by the current. For an intercontact distance $d = 500$ nm, we found in the simulation that energy minimization leads to the nucleation of a fifth vortex with opposite chirality in the matrix centre and four antivortices on the matrix sides, as shown in Fig. 3. The chirality of all the vortices and antivortices is determined by the current polarity.

A necessary condition for phase-locking to occur is that the vortex cores all have the same polarity. In fact, only in this case can they have the same sense of gyrotropic precession[16]. As far as the antivortex polarities are concerned, with the contacts coming closer, the system will tend to reduce its magnetostatic energy by closing the stray field through the cores. Given a ratio of $\sqrt{2}$ in the distance between the nearest vortex–vortex neighbours and the nearest vortex–antivortex neighbours, each vortex closes the stray field mainly through the nearest-neighbour antivortices and vice versa. As a consequence, the most energetically favourable configuration in the absence of an external field and at zero temperature is the antiferromagnetic chessboard. Exchange energy does not change with the polarity configuration and, therefore, does not determine the ground state. At room temperature, the maximum intercontact distance at which this condition is satisfied can be estimated by comparing the far-field dipolar energy of the system with the thermal energy[17,18]. The dipolar energy in a vortex–antivortex pair can be estimated in the following way. In a vortex (antivortex) the out-of-plane magnetization is significantly different from zero only in the core region. Thus, over distances much larger than the core size, the stray field can be written as the field generated by a dipole of magnetic moment μ (refs 17, 19).

$$\boldsymbol{\mu} = \mu\hat{\boldsymbol{z}}; \quad \mu = VM_S \approx \pi l_{ex}^2 L M_S \tag{1}$$

where M_S is the saturation magnetization, $\hat{z}$ is the direction perpendicular to the plane and V is the core volume calculated by multiplying the film thickness L by the core area, assuming a core radius equals to the exchange length l_{ex}. Consequently, the characteristic scale of the vortex–antivortex long-range dipolar energy is given by

$$U_{dip} \approx \frac{\mu^2}{\delta^3} \tag{2}$$

with δ being the vortex–antivortex distance. The associated characteristic temperature $T_{dip} = U_{dip}/k_B$, with k_B being the Boltzmann constant, is equal to room temperature for $\delta \approx 215$ nm. This estimation is consistent with our observation of phase-locking at room temperature for intercontact distance $d = 500$ nm.

Although the antiferromagnetic chessboard is stabilized by the dipolar interaction between vortices and antivortices, this interaction, for the rather large intercontact distances considered here, is not strong enough to keep the vortices phase-locked. In fact, the long-range exchange interaction between a vortex and the nearest-neighbour antivortex is[16]

$$U_{ex} = AL \ln \frac{\delta}{\nu} \tag{3}$$

where A is the exchange constant, $\nu = 2l_{ex}$ is the size of the vortex core, and δ is assumed to be equal to 250 nm. The exchange energy is $U_{ex} = 1.4 \times 10^{-18}$ J, which is about three orders of magnitude larger than the long-range dipolar energy estimated through equation (2) at the same distance. This means that the vortex coupling is due to the balance between the restoring force exerted by the periodic Oerstead potential and the attractive forces between vortices and antivortices due to the exchange interaction.

The exchange interaction between the vortices and their surrounding antivortices forces the former to precess on a larger orbit, with a consequent reduction of the detected output frequency and tunability in current. This reduction does not seem to be directly related to the phase-coupling but simply to the reduction of d, and, hence, of the vortex–antivortex distance. In fact, a reduction of frequency and tunability is also observed when decreasing the intercontact distance from $d = 10\ \mu$m to $2\ \mu$m.

The vortex–antivortex stray field at a distance $\delta = 250$ nm is rather small, that is, $\sim$0.01 mT calculated as U_{dip}/μ. Therefore, in principle, any perpendicular field larger than this, applied during

nucleation, should inhibit the formation of the antiferromagnetic chessboard. In contrast, we have already shown in Fig. 2f that condensation occurs in a much larger range of $H_{\perp}$.

The behaviour in the presence of a perpendicular applied field can be understood with the help of a dynamic micromagnetic simulation. When a field is applied perpendicular to the plane during nucleation of the vortices, the static ground state is one of the ferrimagnetic configurations[17]. For instance, in a simplified system of two contacts, if a field of +1 mT is applied, all the vortices and antivortices nucleate with the core polarities oriented as the field (see Supplementary Video 1). During their incoherent oscillation, the distance between vortices and anti-vortices periodically falls below $d/2$, causing an increase in the energy of the system. In a certain range of externally perpendicular applied d.c. fields, this distance can be sufficiently small that the energy of the ferrimagnetic configuration is dynamically larger than that of the antiferromagnetic chessboard. As a consequence, the system goes into the antiferromagnetic state by switching of the antivortex core. In the experiment, the transient occurs on a timescale much smaller than the acquisition time, and hence is not recordable during spectrum acquisition.

This switching mechanism has some similarities with the recently discovered switching of a vortex core through bursts of a.c. field[20] or a.c. current[21]. In references 20 and 21, the authors demonstrate that the topology of an orbiting vortex changes when its velocity approaches a critical value. Regions with magnetization opposite to that of the core polarity appear. In these conditions, the field amplitude needed to switch the vortex core is strongly reduced compared to the case of a static vortex. In our system, the stray field of the orbiting vortex indeed acts as an a.c. local field on the antivortex core (and vice versa). However, our simulations suggest that the topological change of the antivortex structure, which allows its core switching with the small field bursts provided by the orbiting vortices, is caused by the exchange interaction with the approaching vortices rather than by dynamic self-deformation when reaching a critical velocity.

In the presence of an in-plane field during nucleation, the spectrum map becomes very rich, as shown in Fig. 4a. The observed multiple peaks are clearly correlated. For instance, at $I_{d.c.} = 27.5$ mA, where four peaks can be observed (Fig. 4b), they are symmetric around the oscillation frequency of the locked mode in the same field conditions with the system previously stabilized in zero in-plane field. The total integrated power is 83 ± 2 nW A^{-2}, that is equal to that measured in the locked state and not a quarter of it, as would be the case if the spectrum were simply the superposition of the signals generated by four vortices independently orbiting around the contacts. Moreover, we emphasize that for other current values (see Fig. 4a) or in-plane applied fields (see Supplementary figure), a different number of modes appear in the spectrum. This implies that the number of excited eigenmodes is not related to the number of nanocontacts.

The effect of an in-plane field can be understood once again with the help of a dynamic micromagnetic simulation. The in-plane field $H_{\parallel}$ elongates the orbits and off-centres them along the plane direction perpendicular to $H_{\parallel}$ (see Supplementary Video 2). This is equivalent to symmetry breaking. By making the two-dimensional potential asymmetric, the strong nonlinear system can be driven from a locked to a free-running mode[22,23]. For instance, if one considers a vortex on the corner of the matrix in Fig. 3 and its two neighbouring antivortices, elongation makes antiparallel alignment more favourable for one of the two antivortices. In this condition, the system can go cyclically through several lowest energy ferrimagnetic states, represented by different ferrimagnetic polarization configurations. Because the power spectrum is acquired on a timescale much larger than the cycling time, the eigenfrequencies corresponding to the ferrimagnetic eigenstates appear simultaneously in the power spectrum, but in reality they are not coexistent.

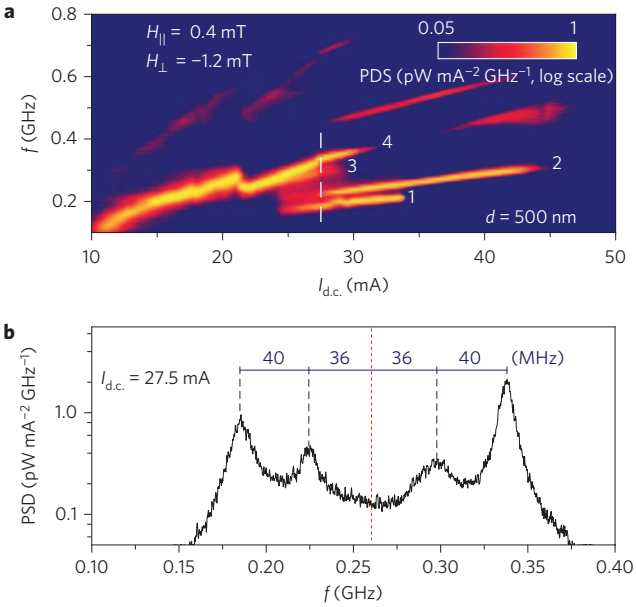

Figure 4 | In-plane field excitation of system eigenmodes. a, Map of power spectrum amplitude versus frequency and applied current bias $I_{d.c.}$ for a matrix of 2 × 2, 500-nm-spaced nanocontacts in magnetic field $(H_{\parallel}, H_{\perp}) = (0.4, -1.2)$ mT. The field is applied before applying the current. The application of the in-plane field component during the initial transient inhibits locking. **b**, Plot at $I_{d.c.} = 27.5$ mA. Four peaks are present that are symmetric around the frequency of the locked state (red dotted line) in the same field with the in-plane field being applied after stabilizing the locked state in a perpendicular field.

Dynamics of interacting solitons, a laboratory system

Let us finally point out that, if one considers a matrix with a much larger number of contacts, it has been theoretically proved[16] that our system is formally equivalent to a variety of two-dimensional systems, such as superfluid films and two-dimensional magnets. In fact, a transition to the superfluid phase occurs when pairs of vortex and antivortex appear, and eventually condensate into a vortex–antivortex square lattice. The transition is called the Berezinskii–Kosterlitz–Thouless (BKT) transition[24] and can be regarded as the two-dimensional counterpart of a Bose–Einstein condensation (BEC)[25,26]. BKT (as well as BEC) transitions are experimentally observed when two conditions are satisfied: the solitons are prevented from spreading by attracting them into potential wells, and at the same time, the solitons are prevented from shrinking by stirring the condensate. The vortices generated by the d.c. current in our array of nanocontacts are prevented from spreading by the force due to the periodic Oersted potential. Because the d.c. current is spin-polarized by the second ferromagnetic layer, the spin transfer torque provides the stirring force on the vortices. The theory of two-dimensional solitons strictly applies because the vortices precess in a continuous film[27]. If the precessing vortices interact through antivortices, phase-locking can be used to model a BKT transition.

Methods

For the devices preparation, the multilayer tantalum (5 nm)/copper (40 nm)/permalloy (4 nm)/gold (6 nm) was deposited on a silicon substrate by d.c. magnetron sputtering (without breaking vacuum) in an argon atmosphere. A resist was spun on the sample for subsequent conductive tip AFM indentation. The resist thickness was tuned to be 40 nm by diluting it with solvent. A voltage of 4 V was applied between the tip and the sample during indentation. By monitoring the tip–sample resistance, the indentation could be stopped when the distance between the tip and the surface of the sample was a few nanometres. The sample was then transferred back in the vacuum chamber where the holes were enlarged and the sample surface reached by etching the resist in 15 W O_2 plasma for 45 s. Without

breaking vacuum, the cobalt (15 nm) / gold (100 nm) top electrode was deposited. Finally, the top electrode was defined by ion milling with real-time monitoring by mass spectroscopy.

For high-frequency measurements, the total direct current $I_{d.c.}$ was applied to the contact matrix through a bias tee. The excited oscillation voltage was amplified (25 dB) and recorded with a commercial spectrum analyser. The shown power spectra were extracted from those recorded by, subsequently, subtracting a reference spectrum measured at $I_{d.c.} = 0$ mA in the same magnetic field conditions and removing the amplification.

A field of 0.7 T was applied out of the sample plane as a reset field before acquisition of each spectrum. The polarity of this field defines the positive field direction. In all the shown spectra, the magnetic field is always applied before applying the current.

The micromagnetic simulations were performed with the public code OOMMF. The simulations included the Oersted field due to the current. For calculation of this field, we assumed the infinite wire approximation with current density constant in the area of the contacts. A cell size of 2.5 nm × 2.5 nm × 5 nm was used for the simulation shown in Fig. 3 and Supplementary Video 2, and 5 nm × 5 nm × 5 nm for Supplementary Video 1. We used the following material parameters for cobalt: saturation magnetization $M_S = 1.4 \times 10^6$ A m^{-1}, exchange constant $A = 3 \times 10^{-11}$ J m^{-1}. Thus, the exchange length was calculated to be $l_{ex} = \sqrt{2A/\mu_0 M_S^2} = 5$ nm. A damping constant $\alpha = 0.01$ and a polarization $P = 0.3$ were used in the dynamic simulations.

Received 27 March 2009; accepted 5 May 2009; published online 21 June 2009

References

1. Shinjo, T., Okuno, T., Hassdorf, R., Shigeto, K. & Ono, T. Magnetic vortex core observation in circular dots of permalloy. *Science* **289,** 930–932 (2000).
2. Wachowiak, A. *et al.* Direct observation of internal spin structure of magnetic vortex cores. *Science* **298,** 577–580 (2002).
3. Pribiag, V. S. *et al.* Magnetic vortex oscillator driven by d.c. spin-polarized current. *Nature Phys.* **3,** 498–503 (2007).
4. Slonczewski, J. C. Current-driven excitation of magnetic multilayers. *J. Magn. Magn. Mater.* **159,** L1–L7 (1996).
5. Berger, L. Emission of spin waves by a magnetic multilayer traversed by a current. *Phys. Rev. B* **54,** 9353–9358 (1996).
6. Katine, J. A., Albert, F. J., Buhrman, R. A., Myers, E. B. & Ralph, D. C. Current-driven magnetization reversal and spin-wave excitations in Co/Cu/Co pillars. *Phys. Rev. Lett.* **84,** 4212–4215 (2000).
7. Grollier, J. *et al.* Spin-polarized current induced switching in Co/Cu/Co pillars. *Appl. Phys. Lett.* **78,** 3663–3665 (2001).
8. Tsoi, M. *et al.* Excitation of a magnetic multilayer by an electric current. *Phys. Rev. Lett.* **80,** 4281–4284 (1998).
9. Kiselev, S. I. *et al.* Microwave oscillations of a nanomagnet driven by a spin-polarized current. *Nature* **425,** 380–383 (2003).
10. Pufall, M. R., Rippard, W. H., Schneider, M. L. & Russek, S. E. Low-field current-hysteretic oscillations in spin-transfer nanocontacts. *Phys. Rev. B* **75,** 140404(R) (2007).
11. Mistral Q. *et al.* Current-driven vortex oscillations in metallic nanocontacts. *Phys. Rev. Lett.* **100,** 257201 (2008).
12. Mancoff, F. B., Rizzo, N. D., Engel, B. N. & Tehrani, S. Phase-locking in double-point-contact spin-transfer devices. *Nature* **437,** 393–395 (2005).
13. Kaka, S. *et al.* Mutual phase-locking of microwave spin torque nano-oscillators. *Nature* **437,** 389–392 (2005).
14. Bouzehouane, K. *et al.* Nanolithography based on real-time electrically controlled indentation with an atomic force microscope for nanocontact elaboration. *Nano Lett.* **3,** 1599–1602 (2003).
15. Georges, B., Grollier, J., Cros, V. & Fert, A. Impact of the electrical connection of spin transfer nano-oscillators on their synchronization: an analytical study. *Appl. Phys. Lett.* **92,** 232504 (2008).
16. Huber, D. L. Dynamics of spin vortices in two-dimensional planar magnets. *Phys. Rev. B* **26,** 3758–3765 (1982).
17. Bishop, J. E. L., Galkin, A. Y. & Ivanov, B. A. Ground states of an array of magnetic dots with Ising-type anisotropy and subject to a normal magnetic field. *Phys. Rev. B* **65,** 174403 (2002).
18. Guslienko, K. Y. Magnetostatic interdot coupling in two-dimensional magnetic dot arrays. *Appl. Phys. Lett.* **75,** 394–396 (1999).
19. Usov, N. A. & Peschany, S. E. Magnetization curling in a fine cylindrical particle. *J. Magn. Magn. Mater.* **118,** L290–L294 (1993).
20. Van Waeyenberge, B. *et al.* Magnetic vortex core reversal by excitation with short bursts of an alternating field. *Nature* **444,** 461–464 (2006).
21. Yamada, K. *et al.* Electrical switching of the vortex core in a magnetic disk. *Nature Mater.* **6,** 269–273 (2007).
22. Paraoanu, G.S. Running-phase state in a Josephson washboard potential. *Phys. Rev. B* **72,** 134528 (2005).
23. Tatarkova, S. A., Sibbett, W. & Dholakia, K. Brownian particle in an optical potential of the washboard type. *Phys. Rev. Lett.* **91,** 038101 (2003).
24. Kosterlitz, M. & Thouless, D. J. Ordering, metastability and phase transitions in two-dimensional systems. *J. Phys. C* **6,** 1181–1203 (1973).
25. Bose, S. N. Plancks gesetz und lichtquantenhypothese. *Z. Phys.* **26,** 178–181 (1924).
26. Anderson, M. H., Ensher, J. R., Matthews, M. R., Wieman, C. E. & Cornell, E. A. Observation of Bose–Einstein condensation in a dilute atomic vapor. *Science* **269,** 198–201 (1995).
27. Guslienko, K. Y. Magnetic vortex state stability, reversal and dynamics in restricted geometries. *J. Nanosci. Nanotech.* **8,** 2745–2760 (2008).

Acknowledgements

A.R. is supported by the the EU network SPINSWITCH (MRTN-CT-2006-035327). The authors acknowledge financial support from the ANR agency (NANOMASER PNANO-06-067-04 and ALICANTE PNANO-06-064-03) and EU grant MASTER No. NMP-FP7-212257.

Additional information

Supplementary information accompanies this paper at www.nature.com/naturenanotechnology. Reprints and permission information is available online at http://npg.nature.com/reprintsandpermissions/. Correspondence and requests for materials should be addressed to A.R.